

UC Santa Cruz

UC Santa Cruz Previously Published Works

Title

New lumped/distributed equivalent circuit based theory for avalanche breakdown suppressed reverse-bias PIN photodetectors

Permalink

<https://escholarship.org/uc/item/0p96n5pr>

Journal

Applied Physics A, 131(4)

ISSN

0947-8396

Authors

Yamada, Hidenori

Yamada, Toshishige

Publication Date

2025-04-01

DOI

10.1007/s00339-025-08361-w

Copyright Information

This work is made available under the terms of a Creative Commons Attribution-NonCommercial-NoDerivatives License, available at <https://creativecommons.org/licenses/by-nc-nd/4.0/>

Peer reviewed

New Lumped/Distributed Equivalent Circuit Based Theory for Avalanche Breakdown Suppressed Reverse-Bias PIN Photodetectors

Hidenori Yamada^{1,2a}, Toshishige Yamada^{3,4a}

¹ Electrical and Computer Engineering, San Diego State University, San Diego, CA 92182, USA

² Electrical and Computer Engineering, University of California San Diego, La Jolla, CA 92092, USA

³ Electrical and Computer Engineering, Baskin School of Engineering, University of California Santa Cruz, Santa Cruz, CA 95064, USA

⁴ Electrical and Computer Engineering, School of Engineering, Santa Clara University, Santa Clara, CA 95053, USA

Abstract: Photodetectors with no illumination must provide zero current for any voltage biasing. Recent experimental work in the literature[1] proposes a new structure to delay the onset voltage of avalanche breakdown. The present authors (HTY) propose a new theory for the recent experimental work, focused on just before the onset of avalanche. The reverse bias of the photodetectors are explicitly considered with device doping information, and how much photon absorption is enhanced, while how much unwanted electron-hole pair recombination is suppressed. HTY consider the insulator in the new structure forces the device current path to go deeper into the bulk, and the longer path effectively suppresses the electric field, thus forcing a higher avalanche onset voltage. HTY further analyze the electric field by using energy band diagrams with quasi-Fermi levels, and also reinterpret the higher voltage as resulting from extra resistive elements, either lumped or distributed, in the equivalent circuit.

Keywords: avalanche breakdown, energy bands, lumped and distributed, equivalent circuits, photodetectors, quasi-Fermi levels, forward and reverse bias, semiconductor doping

I. Introduction

Generally, photodetectors without the illumination input in darkness must provide zero current and power. Here, we discuss the ideal mathematical behavior of photodetectors. Thus, the device output is zero if there is no illumination input[2]. Ideally, no matter how large a voltage is applied to photodetectors, the dark output current should stay zero[3], [4]. However, experimentally, a large enough reverse bias voltage will cause uncontrolled current, even in darkness, through a phenomenon called avalanche breakdown[5].

In their recent works, Goll, Schneider-Hornstein, and Zimmerman have studied PIN photodetectors with physical structures on the top layer involving p^+ and n^+ electrodes and p^- serving as the intrinsic region[1]. They placed a top insulating guard ring and increased the onset of avalanche breakdown, thus increasing the operating window for input voltage before photodetectors generate unwanted malfunctioning.

In this article, HTY propose a new theory to explain the findings of the Austrian group. According to HTY's new theory, the experimental structures to suppress unwanted onset of avalanche breakdown

^a Corresponding authors: hyamada@sdsu.edu, tyamada@soe.ucsc.edu

involves forcing the current to find a path deeper in the *i*-region bulk by placing an insulator between the electrodes. In HTY's theory, PIN photodetectors are discussed exclusively. With high doping, the contacts between external metal wires and the electrodes will make Schottky barriers thinner and will not degrade good contacts[6], [7], [8], [9], [10].

In the pure physics community, theories start with thermal equilibrium as an assumption, far away from avalanche breakdown. The voltage can be included as a chemical potential difference or a Helmholtz free energy difference[11]. Both Kubo's statistical mechanics model[12] and Nyquist's equivalent circuit model[13] carry this thermal equilibrium basis. However, thermal equilibrium conditions are not compatible with the high reverse bias and constant doubling of number of carriers present in the avalanche breakdown discussed.

Experimentally, there is very little difference between the operation modes just before the onset of avalanche breakdown and deep into the breakdown region. Therefore, the measured I-V characteristics will cover both voltage ranges with equal importance, even though there is no theory available for the deep breakdown region. Nonetheless, the threshold voltage, known as the breakdown voltage, can be compared between two different conventional, and newly proposed photodetector structures.

HTY's new theory will focus on the photodetectors just before the onset of the avalanche breakdown. This treatment does not violate the traditional statistical physics requirements for thermal equilibrium[14], [15], [16], while it is not in conflict to good contacts, either. This condition of just before avalanche onset is expressed using energy bands. Lumped and distributed equivalent circuit models are developed for the traditional and the modified devices and explain why the new devices are better. HTY's new equivalent circuit models explain in terms of quasi-Fermi levels in the typical reverse biasing in PIN photodetectors.

Understanding failure modes in sensors is critical. Batteries can be considered as chemical sensors for electrolyte ions, such that input is high energy electrolyte and output is device current[17], [18], [19], [20]. Batteries must avoid low output current for high energy electrolyte. This is the same as photodetectors such that input is illumination and output is device current. Photodetectors must avoid high output current for zero illumination. Understanding failure modes in sensors is related to identifying relevant physical mechanisms in sensing.

Before discussing HTY new theory, optics modeling and electronics modeling are compared, since the HTY new theory takes a position of the latter, the electronics modeling.

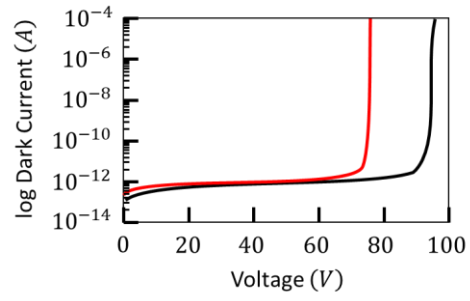
In the photonics community, all research is focused on photon absorption A . First, an incident wave illuminates a device, and photon reflection R and photon transmission T are measured as fractions. Then $A = 1 - R - T$. There is no focus on whether the device is forward or reverse biased or how the semiconductor is doped. Thus, reverse biased photodetectors and forward biased solar cells are discussed as if they were essentially the same device.

In the electronics community, reverse bias photodetectors and forward bias solar cells are considered as drastically different devices. In photodetectors, generated electron-hole pairs are spatially separated thanks to the reverse bias, significantly reducing unwanted electron hole recombination. However, in solar cells, due to forward bias, generated electron-hole pairs are subject to unwanted recombination. In fact, this is calculated as recombination current and is detrimental to good solar cell performance.

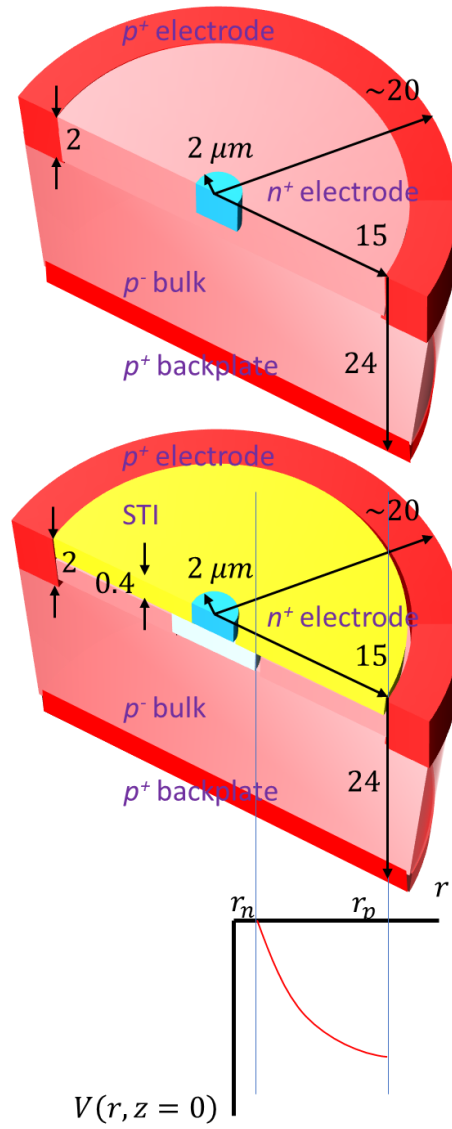
In this manuscript, we will take the electronics view. The reverse bias is explicitly considered in our HTY model alongside doping information. The Austrian experiment operates near or at breakdown voltages, and solid state physics is necessary to discuss why the addition of STI would increase the breakdown voltage for the photodetector. Focusing on photon absorption only would be insufficient.

II. Preview of Final Electric Field Lines

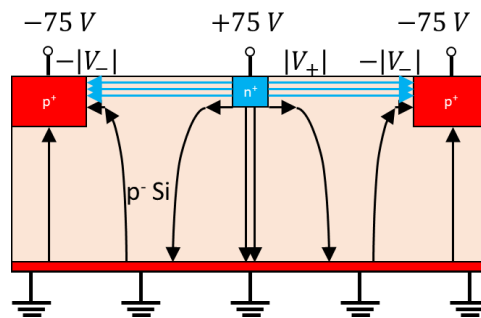
(a)



(b)



(c)



(d)

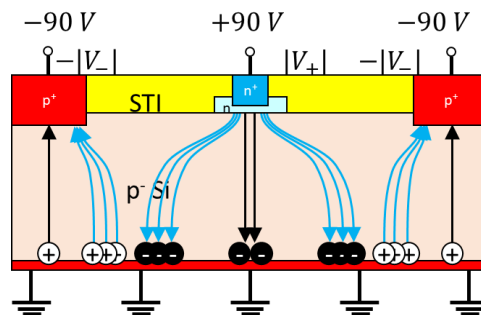


Figure 1. Electric fields within the photodetector under variations in physical structure. (a) A replot of published data: reverse bias photodetector I-V from Austrian group displaying increase in breakdown voltage from 75 V to 90 V. Measurement taken from Ref. [1]. (b) A 3D schematic for the 75 V and 90 V cases, showing the change in physical structure from the 75 V case as an insulator in yellow. (c) With top p^+ electrodes and no shallow trench isolation (STI), the horizontal fields are attracted to the outer electrode ring, and the dominant current path is reinforced to be parallel to the top surface of the photodetector. (d) With top p^+ electrodes and with STI, the vertical fields reach all the way to the bottom p^+ backplate, making the dominant current path perpendicular to the top surface. The polarized induced charges are explicitly drawn on the bottom p^+ backplate. To preserve the ground across the metal surface, different regions have opposite charges on the same backplate.

Previous work[1] on using shallow trench isolation (STI) with radial PIN photodetectors showed suppression of the unwanted avalanche breakdown effect when adding the STI. Fig. 1(a) plots experimental measurements of dark current on log scale vs. reverse bias voltage for the structure shown in Fig. 1(b). This is an engineering test for malfunctions for photodetectors: a photodetector is illumination input and current output, so the “ideal” case would be zero current in dark independent of reverse bias voltage. Instead, the experimental plot shows vertically increasing current on log scale at different voltages for non-STI at 75 V and STI at 90 V.

In HTY’s new theory, we demonstrate that with STI, charges flow from the top n^+ layer at 90 V to the bottom p^+ backplate at 0 V, and then flow from the bottom p^+ backplate at 0 V to the top p^+ at -90 V . Without STI, the charge routes are localized to the surface, starting from the surface n^+ at 75 V and ending at the surface p^+ at -75 V . Everything is based on the fundamental Maxwell’s electromagnetism, such that the electric field is perpendicular to metallic interfaces, where p^+ or n^+ layers correspond to

metallic interfaces. It is the goal of this manuscript to propose physical interpretations for failure modes: avalanche breakdown, combined with an increase in path length with STI. HTY's new theory discusses both the electrostatics cause and an entropy interpretation paying special attention to this path length increase.

The electric field lines in Figs. 1(c)-(d) are conclusions, and the justification will be covered in a later section. In Fig. 1(b), the physical structure of the final device is shown. The top n^+ electrode in cyan is separated from the surrounding top p^+ electrode in deep red by an insulating shallow trench isolation (STI) zone in yellow. Furthermore, there is a grounded bottom p^+ backplate also in deep red at the bottom of the structure, connected to both electrodes with the background p^- wafer in pink. When discussing electric fields for the improved coaxial structures[1], HTY's theory will evolve it from just the top n^+ electrode and bottom p^+ backplate, introducing the STI and p^+ electrode one by one. In similar work involving multiple conductors, coplanar structured 5G devices are discussed. The final electric field is found by superimposing three simpler charged structures in the same way[21] that the n^+ and p^+ electrodes are treated in the present paper.[21]

Without the insulating STI in Fig. 1(c), horizontal fields dominate, and the dominant current path is shown by the horizontal blue arrows. Due to the reverse biasing, the current starts from the top n^+ electrode at +75 V and ends at the top p^+ electrode at -75 V. With the STI in Fig. 1(d), both n^+ and p^+ are located at the top of the device. The current starts from the top n^+ electrode at +90 V, travels through the bottom p^+ backplate at 0 V as a via, and only then ends at the top p^+ electrode at -90 V, thus greatly increasing the physical path length. In the energy band in Fig. 5(c), the current starts from the bottom n^+ electrode at +90 V, travels through the middle p^+ at 0 V as a via, and ends at the top p^+ electrode at -90 V.

The inset plot of Fig. 1(b) is a schematic of the voltage along the boundary between p^- and STI moving from the edges of the top n^+ and p^+ electrodes. In coaxial devices, the electric field decreases in the same way in the radial directions based on the general electromagnetic theory[22]. As the present photodetectors have a coaxial structure, it is expected that the field magnitude will decrease as the radius increases, i.e. near the top p^+ electrode[21], [22]. The top p^+ circular layer thickness for dark PIN devices can be $\sim 5 \mu\text{m}$ as seen in Fig. 1(b). However, if devices need to be optimized for illuminated performance, the thickness possibly needs to be minimized down to 1 or even $0.5 \mu\text{m}$ since the layer reduces the effective area for illumination acceptance.

The layer thickness is related to device design principles. In photodetector device design, the top n^+ in blue and the top p^+ in red need to be as thin as possible so that more illumination can be absorbed by the depletion region in pink. However, if the top n^+ and top p^+ regions are too thin, there is a problem: if we optimize absorption too much, we will lose the vital highly doped regions, and significant voltage drops occur with steep slopes as seen in Fig. 5(d). This is called dielectric breakdown and may result in irreversible damage to the device hardware. This is a tradeoff between more illumination absorption and unwanted onset of dielectric breakdown, which is typical in engineering device design.

The blue layer of Fig. 2(d) has a characteristic depth roughly determined by the top n^+ region thickness. In this paper, we suggested that we can go down to $0.5 \mu\text{m}$ for the top p^+ region thickness, which is a conservative estimate in relation to other photodetector devices. In fact, a 2012 CMOS example already has $0.2 \mu\text{m}$ thickness [23]. As long as the top p^+ region is thicker than the top n^+ , the current path stays at the surface and the device characteristics are improved.

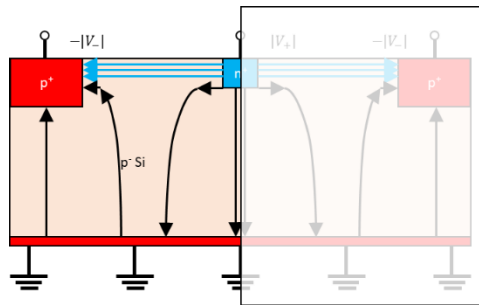
III. Electrostatic Boundary Condition Justification for Section II

Fig. 1(d) displays the induced charges enforced by the grounded bottom. Because the n^+ electrode has heavy positive biasing at +90 V, the bottom at 0 V has negative charges near its center, and the field lines point from positive n^+ to negative charges on bottom. Because the top p^+ electrode has heavy negative biasing at -90 V, the bottom at 0 V has positive charges around its edges, and the field lines point from bottom p^+ backplate to top p^+ electrode. The backplate and electrodes are highly conducting and thus have zero lateral electric field, meaning the field lines must be perpendicular where they hit the surfaces.

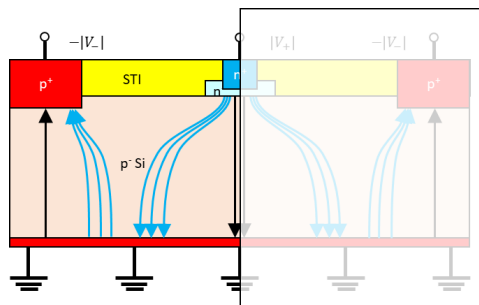
The blue arrows thus represent dominant current paths from n^+ to p^+ as a direct result of the induced bottom charges. These paths are vertical and depend on vertical wafer thickness as opposed to horizontal n^+ to p^+ separation. In Section IV, discussions will be presented on how these longer paths might lead to the same electric field magnitude in relation to avalanche breakdown voltage.

IV. Entropy Interpretation for Section II in Comparison with Experimental Reverse Bias Breakdown Measurements

(a)



(b)



(c)

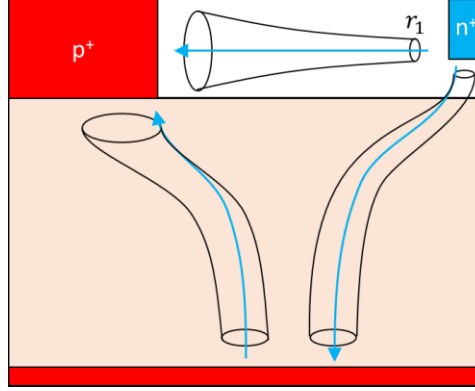


Figure 2. Tracking of the photodetector current cross-section throughout the physical structure. (a) Dominant fields in non-STI photodetectors are mostly horizontal. (b) Dominant fields in STI photodetectors are mostly vertical. (c) The longer vertical path allows for a larger volume of current-relevant regions, resulting in a higher entropy than for the horizontal path.

Fig. 1(d) gives electrostatic mechanisms for why roughly vertical electric fields are created with STI. According to HTY's new theory, there are clear differences in major electron routes for the same device voltages, with traditional non-STI in Fig. 2(a) and new STI in Fig. 2(b). For this discussion, the focus is placed on the cross-section of current carrying charges through the p^- bulk between n^+ and p^+ electrodes.

HTY's entropy-based interpretations are proposed in Fig. 2(c), where the increasing cross-section for the non-STI horizontal electric fields are shown in Fig. 2(a) and for the STI vertical fields in Fig. 2(b). Even with the conservative assumption that the cross-section area is the same for both paths at the p^+ electrode, the longer path has a larger total volume. In the entropy formula

$$S = k_B \ln W, \quad (1)$$

where S is entropy, k_B is the Boltzmann constant, and the number of permutations W . W and S are both extensive variables. Specifically, because permutations usually involve the factorial of the number of elements in the system, the Stirling approximation can be used on a path of \mathcal{L} unit length chunks such that

$$\ln W \propto \ln \mathcal{L}! \approx \mathcal{L} \ln \mathcal{L} - \mathcal{L}. \quad (2)$$

The W term causes entropy to be an extensive variable, dependent on volume. The longer current path length of the STI structure increases the volume of material involved. Thus, the STI version fields result in a higher entropy and are more likely to be the current path[24].

We discuss Helmholtz rather than Gibbs free energies because for most semiconductor device experiments, volume is kept constant rather than pressure [12], [25]. To relate the device voltage V_{dev} to the energy band diagram, it is necessary to discuss the Helmholtz free energy for the n^+ -type at -90 V, $F(n^+, -90$ V), and the p^+ -type at $+90$ V, $F(p^+, +90$ V). If q represents elementary charge 1.6×10^{-19} C, then

$$qV_{dev} = F(n^+, -90$$
 V) - $F(p^+, +90$ V). \quad (3)

This means that qV_{dev} is the difference of the Helmholtz free energies between the reverse biased n^+ and p^+ regions. This is the meaning of the vertical axis in the energy bands.

Under the Fermi-Dirac statistics, the concept of Fermi level (where the distribution function is 50 %) can be extended to the Helmholtz free energy, and this is quasi-Fermi levels. The reverse biased n^+ and p^+ regions have Fermi levels of E_{Fn} and E_{Fp} , respectively. Thus, Eq. 3 can be expressed such that the device voltage is equal to the quasi-Fermi level difference.

The use of entropy makes the Helmholtz free energy conversion nontrivial. Specifically,

$$F = U - TS, \quad (4a)$$

$$S = k_B \ln W. \quad (4b)$$

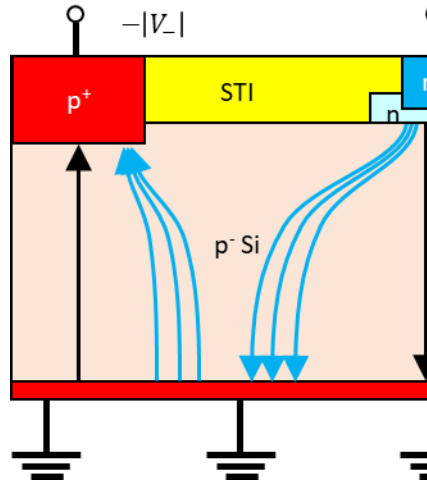
In Eq. (4a), T is the device temperature at 300 K, and S is the device entropy dependent on current path. Calculating the entropy S is a practical problem in device physics. We use the Boltzmann expression in Eq. (4b) defined for the n^+ and p^+ regions, where k is the Boltzmann constant and W is the number of permutations that achieve the given device conditions. For practical calculations, we seldom go back to this original expression except for nanoscale materials, but it is the basis for this theory, and Eq. (3) is the starting point.

The difference in device voltage for the ± 90 V and ± 75 V cases can be assigned to the difference in W for the related paths, under the reasonable assumption that T is the same for both photodetectors. Accordingly, the vertical axis in our energy bands is Eq. (3), which is “the device voltage is the reverse bias Helmholtz free Fermi level difference in n^+ and p^+ regions under the Fermi-Dirac statistics”, or “the quasi-Fermi level differences for reverse biased n^+ and p^+ regions”. This is the meaning of the vertical axis in the energy bands, based on the Shockley and Bardeen energy band theory.

Small electric current flows without illumination. In engineering applications, this non-ideal current is called dark current. In good photodetectors, dark current is used as a figure of merit, i.e., the smaller the dark current is, the better the photodetectors will be. In contrast, photodetector malfunctions occur when there is high runaway device current, at 75 V for non-STI in red and 90 V for STI in black. The current runaway is certainly a malfunction because the device current is high with no applied illumination, i.e. the on state[26]. This is caused by avalanche breakdown, which triggers under a specified electric field for a given semiconductor material. Both non-STI and STI, with their different voltages, must achieve the same trigger electric field within the i -region.

The trigger field for avalanche breakdown in the i -region is determined by the non-STI breakdown voltage. Because there is effectively zero depletion region in the p^+ and n^+ electrodes, the slope can be safely approximated by taking the ratio of the total voltage difference of 75 V and the distance between the electrodes.

(a)



(bi), (bii), (biii)

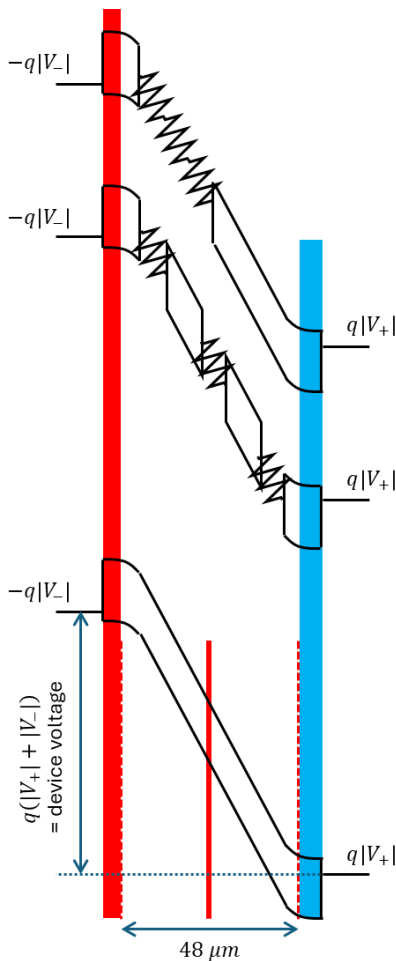


Figure 3. Comparison between (a) real space vertical current path for STI photodetectors and three variants of avalanche onset 90 V reverse biased energy band diagrams: (bi) incorporating a single lumped resistive element to cover the longer length, (bii) incorporating distributed elements, and (biii) an effective energy band that is as wide as the new path length. A lumped model (bi) and a distributed model (bii) are shown schematically. The voltage drop in occurs in a localized way in (bi), but it occurs in a uniform way in (bii). In a realistic distributed model (biii), the horizontal axis starts from the top p^+ , goes down to the bottom

ground n^+ , and then goes up to the top p^+ . The voltage drop is uniform, and the middle point of the horizontal axis is the grounded bottom n^+ .

Fig. 3 addresses the band structure for the STI case. Because the voltage difference is now 90 V, the electric field strength must be reduced by a combination of geometric effects and path length increase as shown in the blue arrows of Fig. 3(a). Put another way, because current is forced to stop over on the bottom on its way from one electrode to the other, the avalanche breakdown voltage must increase.

This can be interpreted as adding a series resistance to the non-STI case, resulting in Fig. 3(bi)-(biii). Note that this has nothing to do with quality of contacts. Instead, the addition of STI can be considered to force extra resistance on the photodetector, thus giving it more of a buffer against extremely high reverse bias voltages. Because the source of resistance is bulk p^- Si, the resistor values are around what might be expected from undoped Si wafers in the vertical direction. The equivalent circuit can therefore be lumped resistive element as in Fig. 3(bi) or distributed resistive element as in Fig. 3(bii).

The lumped element in Fig. 3(bi) groups together the effect of the path extension into one discrete unit. The distributed elements in Fig. 3(bii) split up the lump in Fig. 3(bi), but only three are shown here for mathematical simplicity. Fig. 3(biii) is a more realistic representation of the distributed element case, where there are an infinite number of resistive elements but the resulting device voltage is still 90 V. Because nothing changes about the contact regions on the left and right edges of the diagram, these resistive elements carry the same voltage drop over the same distance as the original depletion region.

For photodetector devices, higher breakdown voltages are generally better because they make malfunctions harder to activate. Fig. 3(biii), which interprets the added resistive elements as an increase in path length, must have the same trigger field as the non-STI case. In a realistic distributed model, the horizontal axis starts from the top p^+ , goes down to the bottom ground n^+ , and then goes up to the top p^+ . The voltage drop is uniform, and the middle point of the horizontal axis is the grounded bottom n^+ .

The STI brings more benefits to PIN photodetectors theoretically, which is to reduce unwanted surface recombination by reducing surface states[27], [28]. The guard ring does not affect unwanted electron-hole recombination. Under the reverse bias, the electron (initial) and the hole (final) are spatially separated. In fact, in Fermi's golden rule to estimate the recombination (transition) rate, a spatial separation in the initial and final states makes the matrix element squared $\langle \psi_f | V | \psi_i \rangle^2$ to be practically zero. Therefore, the reverse-bias electron-hole separation will result in practically negligible recombination. This is in sharp contrast to solar cells, where the forward bias is common and it causes diffusion, allowing unwanted recombination to occur. At this stage, there are experimental results on how much surface states can be reduced by placing the STI.

V. Same Breakdown Electric Field for Different Path Lengths in Section IV Data

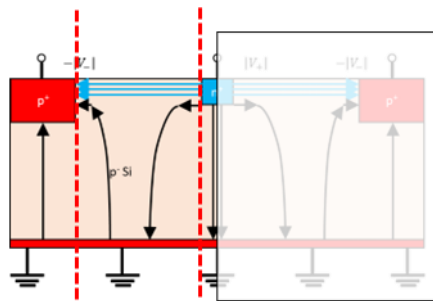
In the optics community, models have no distinction of FB or RB conditions. Photons are considered as traveling waves, and reflection and transmissions are important. Photon waves not reflected nor transmitted must be absorbed, and absorption is the most important figure of merit. For this reason, optics models usually do not incorporate the device biasing conditions such as RB or FB, or

semiconductor doping conditions. Thus, RB photodetectors and FB solar cells are discussed on the same models.

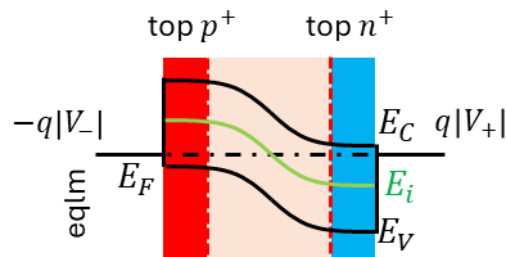
In the electronics community, models have a rigorous distinction of RB for photodetectors and FB for solar cells. This is because scientists want to incorporate carrier transport explicitly. In RB photodetectors, generated electron-hole pairs are quickly separated, and the chances for unwanted recombination are significantly reduced. In FB solar cells, unwanted electron-hole recombination is unavoidable, and this will limit the device performance. In the electronics community, scientists want to consider these effects in detail.

This is why HTY employs the energy band models and visually show the biasing and semiconductor doping information in this manuscript. The vertical axis of energy bands are free energies, and essentially device voltages is shown above.

(a)



(b)



(c)

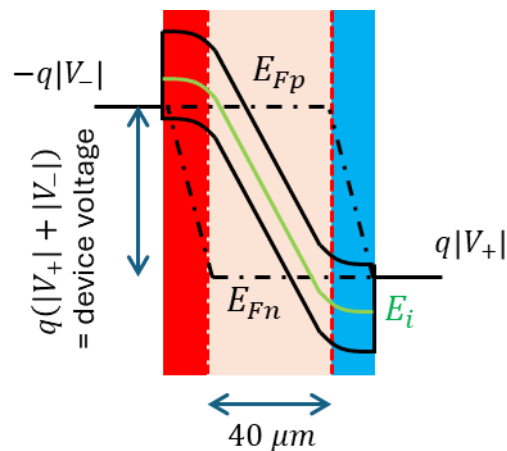


Figure 4. Extracting the electric field that causes the (a) $75 - (-75) = 75 \times 2 \text{ V}$ avalanche onset voltage for non-STI photodetectors. (b) Here, "eqm" is thermal equilibrium. For zero bias, i.e. thermal equilibrium, the electric field should only involve doping concentrations and should not be enough to cause avalanche breakdown. It is nonzero only in the i -region, whose length is synchronized to the real space horizontal field region. (c) For $75 \times 2 \text{ V}$ reverse bias, i.e. onset of avalanche, the electric field is just high enough, i.e. the voltage slope is barely steep enough in the i -region, for electron chain reactions to occur. The necessary quasi-Fermi levels are shown, and the involved depletion region fills the entire i -region. This is a standard device, where the current flows directly from top p^+ to top n^+ without passing through the bottom ground n^+ . Thus, the blue path for the horizontal axis from top p^+ to top n^+ is shorter than for Fig. 5. The vertical axis of energy bands basically corresponds to device voltage. In more detail, the difference of the Fermi level of p^+ and the Fermi level of n^+ is the device voltage. Under illumination or reverse bias, Fermi levels are changed to quasi-Fermi levels, and the same logic is used. The exact horizontal axis widths are labelled with arrows: $40 \mu\text{m}$ for non-STI in Fig. 4(c) and $48 \mu\text{m}$ for STI in Fig. 5(c). The ratio of 40 vs. $48 \mu\text{m}$ between Figs. 4(c),5(c) is exaggerated for visual clarity. The Fermi level splitting shown in the figure thus visually represents the applied reverse bias.

From Fig. 1(a), non-STI photodetectors suffer avalanche breakdown at 75 V . As in Fig. 4(a), when the 75 V reverse bias is applied, the positive terminal is applied to the n^+ electrode, the negative terminal to the p^+ electrode, and the ground to the p^+ backplate. Note the grounded bottom is not part of the conduction path in this scenario. The current conduction path is shown with cyan arrows and covers the horizontal distance between the p^+ and n^+ electrodes. The path is therefore wire, n^+ electrode, p^- , p^+ electrode, wire, and is reflected in the following energy band diagrams. The bottom grounded n^+ does not appear in the energy band.

As in Fig. 4(b), at thermal equilibrium, $np = n_i^2$. Even at zero bias, most of the band bending occurs within the i -region because its resistance is higher than the p^+ and n^+ regions. The i -region electric field is determined solely by Si bandgap and doping. At this point, it has nothing to do with avalanche breakdown.

It is vital to understand that avalanche breakdown is triggered by a critical electric field. Beyond a threshold value, despite reverse biasing, the photodetector device current is high through the mechanism described in Fig. 7[29]. A useful tool to visualize this critical electric field is through the energy band diagram, which tracks Helmholtz free energy F rather than internal energy U as a function of position in photodetectors[12]. Then, the Helmholtz free energy difference is directly related to device voltage $\Delta F = q\Delta V$ where q refers to electron charge. Since HTY's new theory is restricted to just before the onset of avalanche breakdown, energy bands are defined at thermal equilibrium. Avalanche breakdown is certainly not thermal equilibrium, but the applied reverse bias voltage can be included in the chemical potential definition. In such an energy band diagram, the slope of the bending in the i -region is the electric field, so if it is sufficiently steep, avalanche breakdown triggers.

As in Fig. 4(c), at 75 V reverse bias, $np \ll n_i^2$. The i -region electric field at 75 V is meant to be on the threshold of allowing avalanche breakdown. It is the slope of the band in the i -region in Fig. 4(c) that is the critical electric field.

The horizontal axis is shown in terms of length, related to carrier path length through the device. For this purpose, we would like to equate the electric field in non-STI and STI devices. This condition is significant as the onset field strength for breakdown to occur.

For the standard non-STI structure, the horizontal axis range is the path length of around $40 \mu\text{m}$. Without the STI layer, carriers can take a more direct route from p^+ electrode to n^+ electrode without needing to stop at the p^+ backplate. The material breakdown type is most likely avalanche, which is reversible unless applied for an extended duration such that heat damage affects the background p^- doping. This causes unwanted dopant atom migration, i.e. shifting vital atoms around. In the

conventional optics models, dopant atoms are not of interest. However, in EE or semiconductor physics, dopant atoms will define the device structure and play a key role in transport physics. They must be preserved in their initial configuration.

The dielectric breakdown onset field is consistent with the STI case and restricted to around 3.75 V/ μm (37.5 kV/cm): $\frac{75 - (-75) \text{ V}}{3.75 \frac{\text{V}}{\mu\text{m}}} = 40 \mu\text{m}$. Realistically, this is a hybrid between the surface path and the purely vertical STI path.

The flat quasi-Fermi levels extending beyond the bandgap are a matter of ideal mathematical representation. If simulation is performed [30], the resulting quasi-Fermi levels do stay within the bandgap.

In Fig. 4(c), the device has p^+ , reverse biased depletion region, and n^+ . Then within the depletion region,

$$p = n_i e^{\frac{E_i - E_{Fp}}{k_B T}} < n_i, \quad (5a)$$

$$n = n_i e^{\frac{E_{Fn} - E_i}{k_B T}} < n_i, \quad (5b)$$

$$np < n_i^2. \quad (5c)$$

Since $n_i \ll p^+$ and $n_i \ll n^+$, the detailed behavior of the quasi-Fermi levels does not give any differences in computer engineering. However, Shockley's assumption gives a clear guideline to construct energy band diagrams. This situation is shown with numerical examples in Yang-Schroder. The same situation can be found in STI devices in Fig. 5.

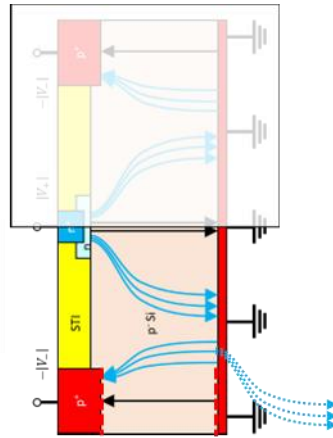
The intrinsic Fermi level for Silicon at 300 K is $\frac{1}{2}(E_C + E_V)$ and the correction reflecting the effective mass difference $\frac{m_C}{m_V}$, where m_C, m_V are conduction and valence band effective masses, is $const \times k_B T \times \ln \frac{m_C}{m_V}$. This const depends on the dimension and the detailed discussion will be a future topic. A rough order estimation is $\frac{1}{2}(E_C + E_V) = 0.55 \text{ eV}$ and the correction is about 0.01 eV, where the top of the valence band is taken as the origin ($E_V = 0$). Thus, in the present HTY's theory, 0.55 eV, the exact half of the silicon band gap 1.12 eV, is used.

In short, E_i basically represents the exact middle line between E_C and E_V in the i -layer. Quasi-Fermi levels are flat in the i -layer because of Shockley's assumption. They are mostly for mathematical idealization, but physically, we can immediately understand whether there the device biasing is forward when E_{Fn} is above E_{Fp} and thus $np > n_i^2$, or reverse when E_{Fn} is below E_{Fp} and thus $np < n_i^2$. We may consider the forward biasing is flooding of charges, and the reverse biasing is drought of charges. This is an immediate benefit of Shockley's assumption. These differences are graphically clear in Fig. 4(c).

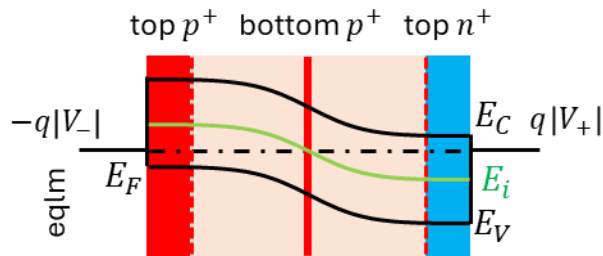
The energy band diagrams emphasize the importance of applied biasing to both avalanche breakdown and recombination, and the quasi-Fermi level separation emphasizes the influence of light illumination. First, if the devices are forward-biased, the depletion region (i.e. sloped region) of the energy band has a shallow slope signifying a weak electric field that cannot separate the electron-hole

pairs before recombination occurs. If the devices are reverse-biased, the depletion region does have a steep enough slope for pair separation. However, if the reverse-bias magnitude is too large, the *i*-layer slope is so steep in the energy band that we have the onset of avalanche breakdown. It is therefore necessary to introduce the guard ring insulator, which expands the width of the energy band diagram and reduces the slope again. Finally, the Fermi level splitting in the energy band indicates the influence of light illumination: if the splitting in the energy band is larger, the device is more sensitive for illumination and is better, and vice versa. The Fermi level splitting can be a figure of merit for illumination sensitivity for devices.

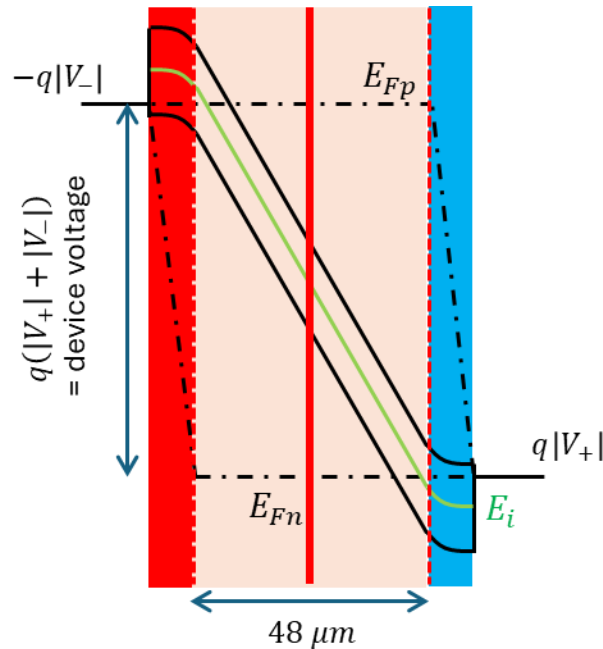
(a)



(b)



(c)



(d)

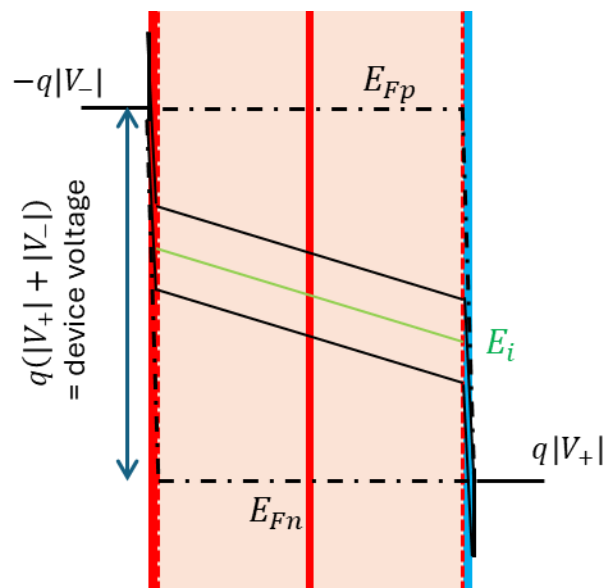


Figure 5. As opposed to the 75 V case, the (a) $90 - (-90) = 90 \times 2$ V avalanche onset voltage for STI photodetectors. (b) Here, “eqm” is thermal equilibrium. For zero bias, i.e. thermal equilibrium, the electric field should only involve doping concentrations and should not be enough to cause avalanche breakdown. In the STI photodiode case, because the path length now stretches over two instances of the photodetector vertical thickness, the *i*-region is significantly wider than that in the 75 V case. (c) For 90×2 V reverse bias, i.e. onset of avalanche, the electric field is just high enough, i.e. the voltage slope is barely steep enough in the *i*-region, for electron chain reactions to occur. Because the *i*-region, equivalently the depletion region, is longer, we need more voltage to achieve the same electric field magnitude. (d) The tradeoff that results from overdoing absorption optimization by making the p^+ and n^+ regions too thin. The vital highly doped regions are lost, and significant voltage drops occur with steep slopes. This is called dielectric breakdown and may result in irreversible damage to the device hardware. This is the STI device, where the current flows top p^+ to bottom ground n^+ , then from bottom n^+ to top n^+ . Thus, the blue path for the horizontal axis from top p^+ to top n^+ is longer than for Fig. 4. The bottom grounded n^+ appears as a mid-point of the horizontal axis in the energy band. The vertical axis of energy bands basically corresponds to device voltage. In more detail, the difference of the

Fermi level of p^+ and the Fermi level of n^+ is the device voltage. Under illumination or reverse bias, Fermi levels are changed to quasi-Fermi levels, and the same logic is used. In other words, (c) is the desired device design reducing breakdown voltage, and (d) is an inappropriate device design focused too much on making the i -region thicker.

From Fig. 1(a), STI photodetectors, unlike non-STI, suffer avalanche breakdown at 90 V. As in Fig. 5(a), the 90 V reverse bias is applied between the n^+ and p^+ electrodes with the p^+ bottom grounded. Unlike the non-STI case, the grounded bottom is certainly part of the conduction path. This time, the cyan arrows representing current conduction path cover double the vertical distance between electrodes and bottom. The path is therefore wire, n^+ electrode, p^- , p^+ backplate, p^- , p^+ electrode, wire. This increases the path length, and so the following energy band diagrams are wider than those in Fig. 5(b)-(c).

As in Fig. 5(b), at thermal equilibrium, $np = n_i^2$. Again, the band bending and therefore electric field is restricted to the i -region. The energy band i -region is slightly wider than double the vertical distance in this schematic to account for the curved nature of the conduction path.

As in Fig. 5(c), at 90 V reverse bias, $np \ll n_i^2$. The i -region electric field at 90 V for STI should be the same as that at 75 V for non-STI as the trigger electric field value for avalanche breakdown. This is possible because of the longer conduction path comparing Fig. 5(a) to Fig. 4(a).

For the STI structure, the horizontal axis range is 48 μm . The STI layer forces a more indirect path, from p^+ electrode to p^+ backplate to n^+ electrode, allowing a longer path length. Once again, a high electric field applied for too long results in dopant migration, which is permanent damage to the device. To preserve the initial dopant configuration, we must again restrict electric field strength to around 3.75 V/ μm : $\frac{90 - (-90) \text{ V}}{3.75 \frac{\text{V}}{\mu\text{m}}} = 48 \mu\text{m}$. That is, the traditional non-STI structure results in the energy band horizontal axis of a shorter 40 μm horizontal axis while the STI structure results in the energy band horizontal axis of a longer 48 μm horizontal axis. The vertical axis of energy bands is the same for both traditional non-STI and the new STI devices as already shown in the figures.

As in Fig. 5(d), with thin n^+ , p^+ regions at 90 V reverse bias, $np \ll n_i^2$. If absorption optimization is overprioritized by making the p^+ and n^+ regions too thin, the vital highly doped regions are lost, and significant voltage drops occur with steep slopes. This is called dielectric breakdown and may result in irreversible damage to the device hardware[31]. This has unavoidable physical consequences if extremely thin layers are used to increase the photon absorption. Obviously, the higher photon absorption using thin surface layers would increase the danger for unwanted dielectric breakdown. For device design, engineers must be aware of this drawback when trying to increase photon absorption. This tradeoff will be a future research topic.

The bottom grounded n^+ appears as a mid-point of the horizontal axis in the energy band. The vertical axis of energy bands basically corresponds to device voltage. In more detail, the difference of the Fermi level of p^+ and the Fermi level of n^+ is the device voltage. Under illumination or reverse bias, Fermi levels are changed to quasi-Fermi levels, and the same logic is used.

To correctly display reverse bias for Fig. 4(c) and Fig. 5(c), quasi-Fermi level rules introduced by Shockley[32] are necessary.

1. E_f stays flat throughout the depletion region.
2. Any change in E_f must occur outside the depletion region.

These rules allow discussion of avalanche breakdown reverse bias voltages in the energy band system developed for thermal equilibrium. Rule 1 allows Fermi level splitting in the depletion region to express the change in np product from n_i^2 . Rule 2 is directly connected to the minority carrier concentration settling down to mass action law mandated bulk values after escaping the depletion region.

Once this calibration is finished, it is straightforward to derive the quantity of " f_t ", which is a frequency with the current amplitude gain is unity. In modern semiconductor device theory, this is more important than " f_{max} ", where the device stops working since electrons cannot respond to quick AC signal back and forth, or power gain is zero. The " f_t " for photodetectors is our main interest, and it has to be emphasized this is derived from the DC characteristics of electron velocity as a function of the electric field. This is also related to the spirit of Prof. Kubo's fluctuation-dissipation theorem.

The reader may consider a photonic version of Prof. Tomonaga's renormalization theory[33] as an extension of this work. That is, bare photons are photons in vacuum, isolated from outside stimuli. In contrast, dressed photons refer to photons being influenced by their environment. In the context of photodetectors, the dressing for dressed photons includes: silicon background, doping, applied reverse bias, electron transport, physical dimensions, and Prof. Bardeen's surface states that help absorb or emit photons (Shockley-Read-Hall recombination). We will write an independent paper and discuss these important problems in the future.

VI. Conclusion

Photodetectors are illumination input and electric current output devices, but there is an equally important aspect important to its speed and sensitivity: the strong reverse biasing. This means that the photodetectors are closer to the avalanche breakdown failure mode if the electric field becomes sufficiently high. It must be considered a failure mode because it will cause nonzero output for zero illumination, i.e. in darkness. The Austrian group performed experiments to try to suppress avalanche breakdown and increase the triggering biasing voltage. The experiments measured both the voltage at the onset of avalanche breakdown as well as the current deep in avalanche condition.

HTY's new theory stops just before the onset of avalanche breakdown. Because avalanche breakdown is triggered by a specific electric field maximum in the semiconductor bulk, the device with the longer current path can absorb a larger voltage at avalanche onset compared to the original. If the scope of the discussion is restricted to onset of avalanche only, it is possible to draw energy band diagrams, based on Kubo's statistical mechanics model, for the onset voltages to visualize the triggering electric field. It is also possible to treat the change in path length as an addition of resistive elements to the Nyquist equivalent circuit of the photodetectors, either lumped or distributed. In this case, the additional series resistance is more related to bulk semiconductor resistance than contact resistance. Although both Kubo and Nyquist models start from thermal equilibrium as a basis, the applied reverse bias can be equated to a condition on the number of carriers in the device through chemical potential.

This concludes HTY's theory for the avalanche breakdown in photodetectors. As an academic interest, how the chain reaction of deep avalanche can be expressed in simulations is an open question and would be a challenge in computer science and engineering.

Acknowledgements: The authors gratefully acknowledge stimulating discussions with Dr. Shih-Yuan Wang and Dr. Ekaterina Ponizovskaya Devine.

Data Availability: All data that support the findings of this study are included within the article (and any supplementary files).

Author Contributions: All authors contributed to conceptualization, data curation, investigation, methodology, formal analysis, and writing. The manuscript has been reviewed by every author.

Ethics Declaration: The authors have no conflicts of interest to disclose.

Appendices

A1. Steady State Input for PIN Photodetectors

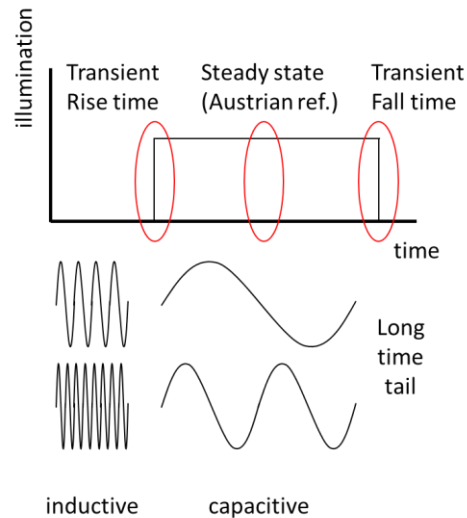


Figure 6. The photodetector response to an incoming signal can be classified into transient or steady-state responses. Transient leads to study of inductive elements and long time tails, which are not the focus of this paper. Instead, HTY's theory focuses on steady-state and assumes all capacitive elements have had time to charge fully, thus creating a meaningful difference in device current paths in the photodetector.

The input to photodetectors can be considered as a rectangular function as in Fig. 6. On the rising edge of the function, the involved frequencies are filtered by the rise time. In optics, special attention is therefore paid to the Fourier series of signal components that survive this rising edge. On the falling edge, the fall time directly influences the so-called long time tail, having to do with how long it takes the output to stop after the input stops. Both types of analyses are transient phenomena in photodetectors. In this case, the device current path does not have time to settle.

In contrast, for the device current centric discussion in this paper as well as the cited experimental data, the focus is on the region between the two edges. The analysis is steady state and avoids both Fourier and the long time tail. In other words, any capacitive elements are fully charged, and the photodetector has had enough time to settle such that there is a meaningful difference between device current paths. It is in this context that the differences between non-STI and STI photodetector structures can be discussed.

A2. Avalanche Breakdown In Energy Bands

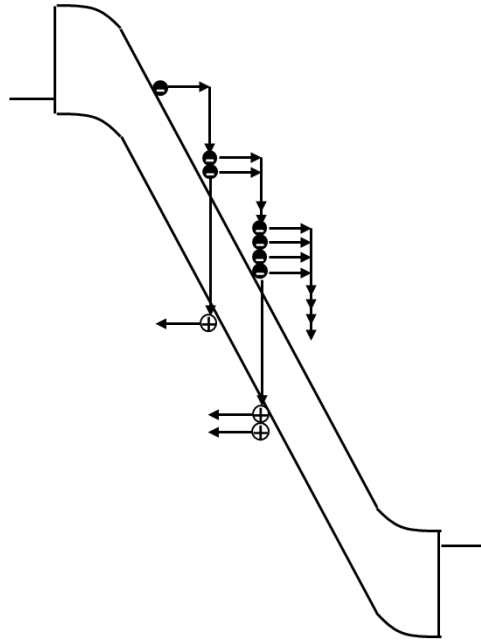


Figure 7. The electron chain reaction, under sufficiently high electric field, unique to avalanche breakdown. This is outside the traditional physics theory assuming the thermal equilibrium. The energy band symbolically shows the chain reaction. Each electron that gains kinetic energy without collisions, i.e. horizontal motion in the conduction band of the energy band diagram, can break a covalent bond and generate an electron-hole pair. This doubles the total number of electrons that contribute to the next step in the chain reaction. This doubling of number of carriers can lead to gains of 10^6 in certain semiconductor structures. The typical silicon mean free path for electrons is 10 nm, or $0.01 \mu\text{m}$ [34]. This is much shorter than the tens of microns represented in Fig. 7, so ballistic transport followed by energy relaxation is practically instantaneous.

The basic mechanism for the avalanche breakdown is a chain reaction. Normally, electron-hole pair generation is thermal excitation of covalent bonds, and pair recombination ensures that the number of available carriers is kept constant over time, i.e. the mass action law. In the case that a large reverse bias voltage is applied and introduces a sufficiently high electric field, electrons can gain enough kinetic energy between natural Ohmic collisions to knock out covalent bonds. The same field still exists for the original and new electrons, and so the number of electrons doubles with a steady interval. This results in massive device current, despite having a reverse bias.

Based on traditional statistical mechanics, this increase in number of electrons is a very difficult issue. Nonetheless, in experiments, avalanche breakdown can be easily observed and measured with a sufficiently high reverse bias voltage. The onset voltage for breakdown can thus be documented as in Fig. 1. The chain reaction can be visualized in energy band diagrams as in Fig. 7 [35].

On the left, the conduction band starts with 1 electron. It gains kinetic energy by moving to the right without following the conduction band. At some point, it collides with a covalent bond to form 1 electron hole pair, thus losing its kinetic energy and moving down vertically. Now there are 2 electrons and 1 hole. The two electrons continue to the right, gaining kinetic energy before losing it in collisions with 2 bonds. Now there are 4 electrons and 2 holes. The next step would end with 8 electrons and 4 holes, and the steps continue until the carriers reach the n^+ Si region to the far right.

The typical silicon mean free path for electrons is 10 nm, or 0.01 μm [34], [36]. This is much shorter than the tens of microns represented in Fig. 7, so ballistic transport followed by energy relaxation is practically instantaneous.

A3. Reversible Breakdown and Avalanche Photodetector Gain

The term “avalanche breakdown” can refer to either reversible or irreversible material breakdown under high voltages. Irreversible breakdown is consistent with the term “dielectric breakdown” when used to refer to solid materials such as Si. This must be contrasted with referring to dielectric breakdown for gases, where it is considered reversible. In this paper, the authors use “dielectric breakdown” to refer to the irreversible solid variety.

For reversible avalanche breakdown, the physical mechanism is as described in Section A2: an exponentially growing chain reaction of electrons creating electron hole pairs out of covalent bonds they collide with. As long as the basic crystal lattice of the solid Si is unaffected, the photodetector can be brought back to normal operation by simply removing the high reverse bias and stopping the chain reaction from starting.

For irreversible avalanche, or dielectric, breakdown, the physical mechanism changes from affecting covalent bonds to affecting atoms. In a phenomenon called migration, entire atoms are moved around until there is a conductive path between the two entry points for the device voltage. Once this happens, this path stays open even after the high reverse bias is removed, and the photodetector loses the ability to turn off permanently. The theory for this type of irreversible breakdown is currently being researched.

Avalanche photodetectors take advantage of the reversible type of breakdown to provide a very high gain at the cost of a high off current. The most sensitive types are called single photon avalanche diodes, or SPADs, with a gain of 10^6 to give appreciable device current for a single incident photon. This high generation of carriers makes Monte Carlo simulations difficult [34], [37]. These million gain photodetectors usually use a *pipn* structure: *i*-region for light absorption and *pn* junction for acceleration. In fact, photodetectors are reverse biased by definition, and gain would be out of scope.

References

- [1] B. Goll, K. Schneider-Hornstein, and H. Zimmermann, "Ultra-Low Capacitance Spot PIN Photodiodes," *IEEE Photonics J.*, vol. 15, no. 2, pp. 1–6, Apr. 2023, doi: 10.1109/JPHOT.2023.3251893.
- [2] C. J. Novotny, E. T. Yu, and P. K. L. Yu, "InP Nanowire/Polymer Hybrid Photodiode," *Nano Lett.*, vol. 8, no. 3, pp. 775–779, Mar. 2008, doi: 10.1021/nl072372c.
- [3] P. Chen *et al.*, "Effects of hydrogen implantation damage on the performance of InP/InGaAs/InP p-i-n photodiodes transferred on silicon," *Appl. Phys. Lett.*, vol. 94, no. 1, p. 012101, Jan. 2009, doi: 10.1063/1.3062848.
- [4] K. B. Quest, "Simulations of High-Mach-Number Collisionless Perpendicular Shocks in Astrophysical Plasmas," *Phys. Rev. Lett.*, vol. 54, no. 16, pp. 1872–1874, Apr. 1985, doi: 10.1103/PhysRevLett.54.1872.
- [5] S. Wu *et al.*, "Ge-on-Si avalanche photodiodes with photon trapping nanostructures for sensing and optical quantum applications," *IEEE Sens. J.*, pp. 1–1, 2023, doi: 10.1109/JSEN.2023.3271215.
- [6] T. Yamada, "Modeling of carbon nanotube Schottky barrier modulation under oxidizing conditions," *Phys. Rev. B*, vol. 69, no. 12, p. 125408, Mar. 2004, doi: 10.1103/PhysRevB.69.125408.
- [7] T. Yamada and D. K. Ferry, "Monte Carlo simulation of hole transport in strained Si_{1-x}Ge_x," *Solid-State Electron.*, vol. 38, no. 4, pp. 881–890, Apr. 1995, doi: 10.1016/0038-1101(94)00123-W.
- [8] W. Lu *et al.*, "InGaN/GaN Schottky Diodes With Enhanced Voltage Handling Capability for Varactor Applications," *IEEE Electron Device Lett.*, vol. 31, no. 10, pp. 1119–1121, Oct. 2010, doi: 10.1109/LED.2010.2058843.
- [9] W. Lu *et al.*, "Analysis of Reverse Leakage Current and Breakdown Voltage in GaN and InGaN/GaN Schottky Barriers," *IEEE Trans. Electron Devices*, vol. 58, no. 7, pp. 1986–1994, Jul. 2011, doi: 10.1109/TED.2011.2146254.
- [10] E. T. Yu, X. Z. Dang, P. M. Asbeck, S. S. Lau, and G. J. Sullivan, "Spontaneous and piezoelectric polarization effects in III-V nitride heterostructures," *J. Vac. Sci. Technol. B Microelectron. Nanometer Struct. Process. Meas. Phenom.*, vol. 17, no. 4, pp. 1742–1749, Jul. 1999, doi: 10.1116/1.590818.
- [11] T. Yamada, H. Yamada, A. J. Lohn, and N. P. Kobayashi, "Room-temperature Coulomb staircase in semiconducting InP nanowires modulated with light illumination," *Nanotechnology*, vol. 22, no. 5, p. 055201, Dec. 2010, doi: 10.1088/0957-4484/22/5/055201.
- [12] R. Kubo, H. Ichimura, T. Usui, and N. Hashitsume, *Statistical Mechanics*, 1st edition. Amsterdam: North Holland, 1990.
- [13] Y. Taur and T. H. Ning, *Fundamentals of Modern VLSI Devices*, 2nd edition. Cambridge: Cambridge University Press, 2013.
- [14] H. Nyquist, "Regeneration theory," *Bell Syst. Tech. J.*, vol. 11, no. 1, pp. 126–147, Jan. 1932, doi: 10.1002/j.1538-7305.1932.tb02344.x.
- [15] M. S. Lundstrom, "On the mobility versus drain current relation for a nanoscale MOSFET," *IEEE Electron Device Lett.*, vol. 22, no. 6, pp. 293–295, Jun. 2001, doi: 10.1109/55.924846.
- [16] M. Lundstrom, *Fundamentals of Carrier Transport*, 2nd edition. Cambridge University Press, 2009.
- [17] H. Yamada and P. R. Bandaru, "Enhanced electrical current densities in electrochemical systems through the use of nanostructured electrodes," *Appl. Phys. Lett.*, vol. 104, no. 21, p. 213901, May 2014, doi: 10.1063/1.4879837.
- [18] H. Yamada and P. R. Bandaru, "Limits to the magnitude of capacitance in carbon nanotube array electrode based electrochemical capacitors," *Appl. Phys. Lett.*, vol. 102, no. 17, p. 173113, Apr. 2013, doi: 10.1063/1.4803925.

- [19] H. Yamada, R. Narayanan, and P. R. Bandaru, "Electron tunneling in nanoscale electrodes for battery applications," *Chem. Phys. Lett.*, vol. 695, pp. 24–27, Mar. 2018, doi: 10.1016/j.cplett.2018.01.054.
- [20] H. Yamada and P. R. Bandaru, "Electrochemical kinetics and dimensional considerations, at the nanoscale," *AIP Adv.*, vol. 6, no. 6, p. 065325, Jun. 2016, doi: 10.1063/1.4955049.
- [21] H. Yamada, "Skin effect suppression for millimeter-wave frequencies through manipulation of permeability," *Eng. Res. Express*, vol. 5, no. 1, p. 015079, Mar. 2023, doi: 10.1088/2631-8695/acc2a2.
- [22] F. Ulaby and U. Ravaioli, *Fundamentals of Applied Electromagnetics*, 7th edition. Boston: Pearson, 2014.
- [23] M.-J. Lee, H. Rucker, and W.-Y. Choi, "Effects of Guard-Ring Structures on the Performance of Silicon Avalanche Photodetectors Fabricated With Standard CMOS Technology," *IEEE Electron Device Lett.*, vol. 33, no. 1, pp. 80–82, Jan. 2012, doi: 10.1109/LED.2011.2172390.
- [24] H. Yamada and T. Yamada, "A semiconductor physics based model for thermal characteristics in electronic electrolytic energy storage devices," *J. Appl. Phys.*, vol. 129, no. 17, p. 174501, May 2021, doi: 10.1063/5.0036639.
- [25] H. Takahashi, *Electromagnetism (電磁気学)*. Tokyo: Syokabo, 1959.
- [26] T. Yamada *et al.*, "Modeling of nanohole silicon pin/nip photodetectors: Steady state and transient characteristics," *Nanotechnology*, vol. 32, no. 36, p. 365201, Jun. 2021, doi: 10.1088/1361-6528/abfb98.
- [27] J. Bardeen, "Surface States and Rectification at a Metal Semi-Conductor Contact," *Phys. Rev.*, vol. 71, no. 10, pp. 717–727, May 1947, doi: 10.1103/PhysRev.71.717.
- [28] T. Yamada, C. W. Bauschlicher, and H. Partridge, "Substrate for atomic chain electronics," *Phys. Rev. B*, vol. 59, no. 23, pp. 15430–15436, Jun. 1999, doi: 10.1103/PhysRevB.59.15430.
- [29] D. K. Schroder, *Advanced Mos Devices*, Reprint Edition. Reading, Mass: Addison-Wesley, 1987.
- [30] X. Yang and D. K. Schroder, "Some Semiconductor Device Physics Considerations and Clarifications," *IEEE Trans. Electron Devices*, vol. 59, no. 7, pp. 1993–1996, Jul. 2012, doi: 10.1109/TED.2012.2195011.
- [31] S. M. Sze and K. K. Ng, *Physics of Semiconductor Devices*, 3rd Edition. Hoboken, N.J: Wiley-Interscience, 2006.
- [32] W. Shockley, "The Theory of p-n Junctions in Semiconductors and p-n Junction Transistors," *Bell Syst. Tech. J.*, vol. 28, no. 3, pp. 435–489, 1949, doi: 10.1002/j.1538-7305.1949.tb03645.x.
- [33] S. Tomonaga, "On a Relativistically Invariant Formulation of the Quantum Theory of Wave Fields*," *Prog. Theor. Phys.*, vol. 1, no. 2, pp. 27–42, Aug. 1946, doi: 10.1143/PTP.1.27.
- [34] D. K. Ferry, *Semiconductors*. New York: Prentice Hall, 1991.
- [35] D. K. Schroder, *Semiconductor Material and Device Characterization*, 3rd edition. Piscataway, NJ : Hoboken, N.J: Wiley-IEEE Press, 2015.
- [36] D. K. Ferry and R. O. Grondin, "An Introductory Review," in *Physics of Submicron Devices*, D. K. Ferry and R. O. Grondin, Eds., Boston, MA: Springer US, 1991, pp. 1–49. doi: 10.1007/978-1-4615-3284-2_1.
- [37] T. Yamada and D. K. Ferry, "Coupled molecular-dynamics Monte Carlo study of the transport properties of lateral surface superlattices," *Phys. Rev. B*, vol. 47, no. 11, pp. 6416–6426, Mar. 1993, doi: 10.1103/PhysRevB.47.6416.